Enhancing the thermoelectric performance of BiGa$_2$X$_4$ (X=S, Se) P-type semiconductors by optimizing charge carrier concentration or chemical potentials

Ahmad Telfah [a,b,c,*], T. Ghellab [d,e], Z. Charifi [d,e], H. Baaziz [d,e], A.M. Alsaad [f], Sahar Abdalla [g,h], Wai-Ning Mei [c], R.F. Sabirianov [c]

[a] *Fachhochschule Dortmund University of Applied Sciences and Arts, Sonnenstrasse 96-100, 44139, Dortmund, Germany*
[b] *Department of Physics, Yarmouk University (YU), Irbid, Jordan*
[c] *Department of Physics, University of Nebraska at Omaha, Omaha, NE, 68182, USA*
[d] *Department of Physics, Faculty of Science, University of M'sila, 28000, M'sila, Algeria*
[e] *Laboratory of Physics and Chemistry of Materials, University of M'sila, M'sila, Algeria*
[f] *Department of Physical Sciences, Jordan University of Science & Technology, P.O. Box 3030, Irbid, 22110, Jordan*
[g] *Chemistry Department, College of Science, Imam Mohammad Ibn Saud Islamic University (IMSIU), Riyadh, 11623, Saudi Arabia*
[h] *Department of Chemistry, Faculty of Science, University of Khartoum, P.O. Box 321, Khartoum, Sudan*

ARTICLE INFO

ABSTRACT

We present an extensive analysis of the structural, electronic, optical, elastic, and thermoelectric properties of *BiGa$_2$X$_4$* compounds, where X represents either sulfur (S) or selenium (Se). Our approach employed the all-electron full potential linearized augmented plane wave (FP-LAPW) technique, offering a comprehensive understanding of these materials' characteristics. The calculated lattice constants (*a*), the unit cell height (*c*), and the c/a ratio closely match experimental data, affirming the accuracy of our calculations. A pivotal focus of our study was on the electronic properties, including the indirect bandgaps (A → M − Γ) and (M → A). We found that BiGa$_2$S$_4$ exhibited an indirect bandgap (*E$_g$*) of 2.504 eV, while BiGa$_2$Se$_4$ possessed a slightly lower value of 1.878 eV. This variation was primarily attributed to the intricate interactions among bismuth, sulfur, and selenium atoms, particularly involving $p - p$ orbital interactions. Additionally, we explored the optical characteristics of these compounds, determining their maximum absorption wavelengths. *BiGa$_2$S$_4$* exhibited an absorption peak at 4.476 eV, whereas *BiGa$_2$Se$_4$* displayed a slightly lower maximum absorption at 3.741 eV. Moreover, *BiGa$_2$Se$_4$* showcases a higher dielectric constant, which augments its potential for optoelectronic applications. A critical aspect of our research is the assessment of the elastic properties, elucidating that both compounds exhibited fragility and anisotropy. We observed that at 300 K, the lattice thermal conductivity (*k$_L$*) for *BiGa$_2$S$_4$* and *BiGa$_2$Se$_4$* was measured at 1.57 W/mK and 1.14 W/mK, respectively, indicating low thermal conductivity. At 1000 K, both *BiGa$_2$S$_4$*, and *BiGa$_2$Se$_4$* exhibit significant ZT values of 0.8389 and 0.8722, respectively. The ZT values of the *p*-type semiconductors are notably higher than those of the *n*-type. At T = 900 K, the optimized ZT values for *BiGa$_2$S$_4$*, and *BiGa$_2$Se$_4$* are found to be 0.82909 and 0.90548, respectively. Achieving these values requires either increasing the concentration of charge carriers to $n = 0.11715 \times 10^{22}$ cm^{-3} for *BiGa$_2$S$_4$* and $n = 0.0812 \times 10^{22}$ cm^{-3} for *BiGa$_2$Se$_4$*, or reducing the chemical potentials by 0.40151 Ryd and 0.38001 Ryd, respectively.

1. Introduction

Perovskites and inorganic quantum dot solar cells are currently among the most popular and efficient photovoltaic (PV) technologies [1]. These technologies have garnered significant attention due to their potential for cost-effectiveness, compact size, and higher efficiency across a wider spectrum of light intensities compared to existing or emerging technologies. As a result, they are considered as promising

---

candidates for various applications [2,3]. Lead-based materials, exemplified by PbS, CsPbI$_3$ in quantum dot solar cells, and APbI$_3$ (with A representing methylammonium or formamidinium) in perovskite solar cells, have shown remarkable device performance [4–6], However, their wide-ranging application is restricted by their considerable toxicity. Lead is prominently featured on the World Health Organization's list of the top 10 chemicals of substantial public health concern, and it is subject to legal restrictions across the globe [7] Consequently, their potential adoption for the commercial production of solar cells is problematic [8].

Bismuth-based materials emerge as credible substitutes for lead-containing compounds. Bismuth, abundant in the Earth's crust, is readily accessible as a byproduct of lead, copper, and tin refining, and maintains a consistently affordable price [2,3,9]. Remarkably, despite its classification as a heavy metal, bismuth is known for its non-toxic properties and is employed in widely used medications like Pepto-Bismol [10]. Furthermore, Bi3+ has been proposed as an appealing choice for defect-tolerant materials, showcasing exceptional optoelectronic capabilities despite the presence of imperfections. The theory postulates that the active ns$_2$ lone pair in Bi^{3+} fosters the creation of antibonding interactions near the valence band maximum, effectively confining defects to shallow states at the band boundaries [11,12]. Materials categorized as thermoelectric (TE) have the remarkable capacity to convert one form of energy into another, particularly transforming thermal energy into electrical power. The dimensionless TE figure of merit (ZT) expressed as $ZT = \frac{\sigma S^2 T}{k_{Tot}}$, serves as a pivotal metric for assessing the suitability of materials for TE conversion. Within this equation, S represents the Seebeck coefficient, reflecting the voltage generated within materials under a thermal gradient, while σ denotes electrical conductivity. The parameter T signifies absolute temperature measured in Kelvin, and k_{Tot} encompasses the overall thermal conductivity, combining electronic thermal conductivity (k_e) and lattice thermal conductivity parameters [13,14]. The power factor (σS^2) and the overall thermal conductivity of a material stand as vital criteria when selecting a promising TE candidate. TE materials can be categorized based on their operational temperature range, encompassing ambient, mid-temperature, and high-temperature categories. Ultimately, the material's bandgap and stability are the determining factors in its suitability for thermoelectric applications [14].

Bismuth telluride (Bi$_2$Te$_3$) and its alloys (Bi$_{2-x}$Sb$_{2x}$Se$_y$Te$_{3-y}$) have emerged as highly promising bulk thermoelectric (TE) materials for ambient temperature applications, primarily due to their elevated figures of merit, ZT. The *BiGa$_2$X$_4$ (X = S, Se)* compounds meet the criteria for non-toxic composite materials and additionally exhibit noteworthy photovoltaic properties, including significant absorption coefficients, an acceptable bandgap, and remarkable durability. Despite these attributes, these materials have received limited attention. Consequently, strategies that have proven effective in analogous ternary compounds, such as AgBiS$_2$, such as alloying, doping, ligand surface treatment, precise semiconductor alignment, and the formation of bulk heterojunctions, remain largely unexplored [15–18]. Further research in these areas, leveraging this abundant, non-toxic chemical, has the potential to enhance the efficiency of electronic devices. Bismuth-based materials, including photodetectors, hold promise for diverse optoelectronic devices [19–21]. Moreover, these compounds find applications in photocatalytic reactions, including solar-driven hydrogen production and the degradation of light pollutants [22–24]. They are also suitable for use in batteries and clean energy-driven thermoelectric devices [25–28], as well as therapeutic applications in photothermal and bioimaging devices [29–31]. A deeper understanding of bismuth-based materials in each of these disciplines can lead to more effective exploitation and further enhancement of their potential.

The narrow bandgap *BiGa$_2$X$_4$ (X = S, Se)* solids are characterized by low thermal conductivity, substantial Seebeck coefficients, and excellent electrical conductivity, making them highly advantageous

thermoelectric materials. Notably, in the case of Bi$_2$S$_3$ doped with BiCl$_3$, the calculated merit factor of 0.60 is particularly intriguing [28]. Heavy metal-based power semiconductors find utility in a variety of applications, including scintillation semiconductors, catalysts, thermoelectric devices, and photovoltaics [32,33].

The utilization of thermoelectric (TE) devices is inherently reliant on the attributes of TE materials. Materials featuring high figure-of-merit ZT values have consistently been the central focus of research. Various strategies have been deployed to enhance the ZT value of TE materials, involving the manipulation of their electrical conductivities, thermal conductivities, and Seebeck coefficients. These techniques encompass modulation doping, energy band engineering, nanocomposite materials, two-dimensional nanofilms, and one-dimensional nanowires. Augmenting both the individual and synergistic solutions for improving electrical and thermal characteristics is significant. However, challenges persist, impeding the progress and practical implementation of technology-driven TE approaches. Notably, some thermoelectric materials demonstrate exceptional ZT values within the temperature range of 500–1000 K, but these values substantially diminish at ambient temperature, rendering them unsuitable for practical commercial applications. Additionally, it's essential to acknowledge that many materials exhibiting high ZT values consist of precious metals or elements with toxic properties [34,35].

In recent years, significant strides have been made in the field of advanced materials for energy conversion and spintronic applications. Materials demonstrating favorable thermoelectric and spintronic properties have attracted considerable attention for their potential in efficient energy harvesting and transformative computing technologies. This study focuses on *BiGa$_2$X$_4$ (X = S, Se)* compounds, which exhibit promising thermoelectric characteristics, particularly at elevated temperatures.

To situate our investigation within the broader context of advanced materials, we acknowledge recent studies that highlight the diverse functional properties of related systems. For instance, recent research has explored the influence of spin on the ferromagnetic and thermoelectric behaviors of Sr(V/Cr)$_2$S$_4$, underscoring its potential as a candidate for spintronics [36].

Investigations into 2D MXenes (M$_3$N$_2$, where M = Ti, Hf, Zr, Mo) have leveraged first principles approaches to uncover their energy harvesting capabilities and structural stability, marking them as versatile materials in advanced material science [37].

Rare earth-based Mg-chalcogenides, such as MgDy$_2$(S/Se)$_4$, have emerged as promising contenders for spintronic and thermoelectric applications due to their unique electronic structures and magnetic properties [38].

Moreover, studies on Ba$_2$CrXO$_6$ (X = Ta, W, Re, Os) have meticulously examined their Curie temperatures, spin polarization, and transport behaviors, positioning them at the forefront of spintronic research [39]. Research into the structural, spectral, morphological, and absorption properties of the Ba–Co–In–Fe–O system has also yielded valuable insights into multifunctional oxide materials, highlighting their potential for diverse applications [40].

In this study, we present a DFT-based analysis of the TE properties of *BiGa$_2$X$_4$ (X = S, Se)*. We demonstrate that these materials exhibit low thermal conductivity, significant Seebeck coefficients, and remarkable electrical conductivity. Consequently, the ZT values of these materials can reach 0.9, which is comparable to currently utilized TE materials. Following the applied analysis of the structural, electronic, optical, elastic, and thermoelectric properties of the *BiGa$_2$S$_4$* and *BiGa$_2$Se$_4$* compounds, it is suggested that these novel materials hold promise for various optoelectronic applications, particularly in solar photovoltaic applications. Furthermore, the findings indicate intriguing thermoelectric characteristics for both *p*-type and *n*-type doping scenarios.

2. Calculation methods

The calculations in this study were conducted using the Wien2k computer code based on Density Functional Theory (DFT) [41]. Structural properties were determined using the all-electron full potential linearized augmented plane wave (FP-LAPW) method in combination with the Perdew and Wang local density approximation (LDA) functional [42]. For electronic and optical properties, the modified Becke Johnson (mBJ) semi-local exchange potential was employed [43]. It's noteworthy that mBJ has demonstrated its ability to provide a more accurate bandgap compared to the more common LDA/GGA functionals [44,45]. This orbital-independent potential is known for accurately predicting bandgaps for various materials, including insulators, semiconductors, and highly correlated transition metal oxides [44–46]. The plane wave expansion employed an energy cutoff of 400 Ry, and atomic positions were relaxed until the energy reached 10^{-4} Ryd. Self-consistent calculations were carried out with charge and atomic force convergence criteria of 0.001 e and 0.05 mRy/a.u, respectively. The convergence concerning basis size was determined by the lowest muffin-tin sphere radius multiplied by the largest plane wave vector, which was found to be $R_{MT}^{min} \times K_{MAX} = 8$. In computations related to optical characteristics, 20,000 k-points were utilized. Additional settings encompassed $G_{max} = 12$ a.u^{-1} (plane wave cutoff) and R.M.T values

ranging from 0.8 to 1.6 atomic units (a.u) for the atoms (Bi, Ga, S, and Se). For a more efficient investigation of transport parameters, a set of 10,000 k-points was employed. Assuming a constant relaxation time for charge carriers, the Boltzmann Transport (BolzTrap) method was used to compute the transport properties of the materials [47].

3. Results and discussions

3.1. Structural properties

The two compounds under investigation crystallize in the space group *P4/nnc* (N° 126) with a Pearson symbol of tP28. These compounds are characterized by *trans*-edge linked MX_4 tetrahedral units, which are typical of the SiS$_2$ structure. These units act as the fundamental building blocks, aligning themselves into linear anionic chains. In this crystal structure, the M atoms are situated in two distinct crystallographic layers, each with a unique orientation concerning the *Bi2* dumbbells, as shown in Fig. 1. The structural relaxation was achieved by optimizing forces for all volumes. The calculated atomic coordinates based on LDA approximations are compared to experimental results in Table 1, and the agreement between these results and prior experiments is evident [48]. From a microscopic perspective, comprehending the structural characteristics of solids is of utmost importance.
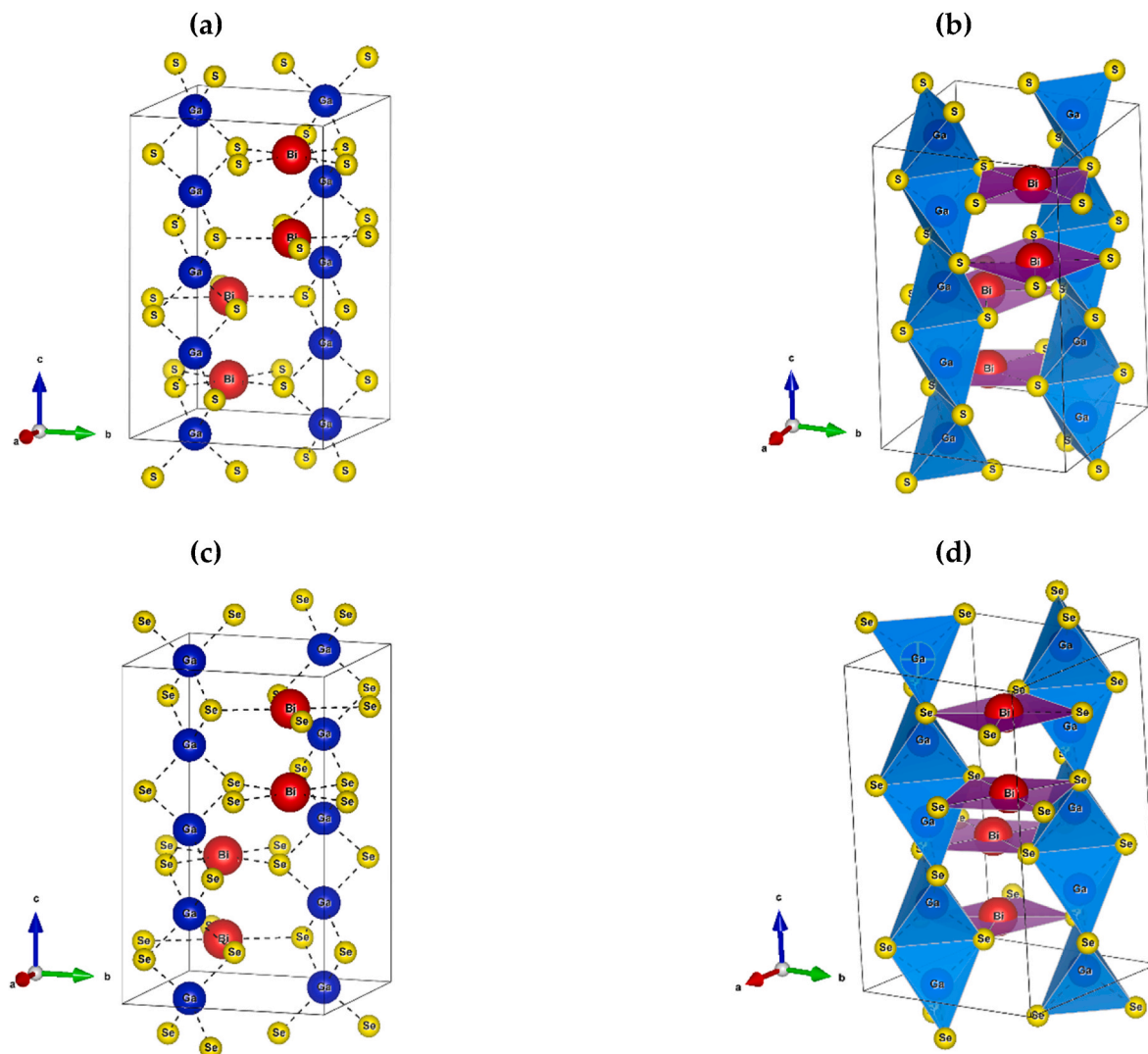
(a)   **(b)**

(c)   **(d)**

Fig. 1. Crystal structure of $BiGa_2X_4$ ($X = S, Se$): (a) and (c) single tetragonal (*P4/nnc* space group) of $BiGa_2S_4$ and $BiGa_2Se_4$ respectively along the (111) plane, (b) and (d) tetrahedral configuration of the groups in $BiGa_2S_4$ and $BiGa_2Se_4$ respectively. Red: Bi; Blue: Ga; Yellow: S, Se.

Table 1

Atomic positions predicted for $BiGa_2X_4$ ($X = S, Se$) with the LDA approximation.

Compounds	Atome	Wyckoff Positions	Atomic positions
$BiGa_2S_4$	Bi	4e	(1/4, 1/4, 0.12096), Exp: (1/4, 1/4, 0.11933) [48].
	Ga (1)	4d	(1/4, 3/4, 0), Exp: (1/4, 3/4, 0) [48].
	Ga (2)	4c	(1/4, 3/4, 3/4), Exp: (1/4, 3/4, 3/4) [48].
	S	16k	(-0.0882, 0.0920, 0.1252), Exp: (−0.0914, 0.0812, 0.1254) [48].
$BiGa_2Se_4$	Bi	4e	(1/4, 1/4, 0.12627), (1/4, 1/4, 0.12422) [48].
	Ga (1)	4d	(1/4, 3/4, 0), (1/4, 3/4, 0) [48].
	Ga (2)	4c	(1/4, 3/4, 3/4), (1/4, 3/4, 3/4) [48].
	Se	16k	(-0.0809, 0.0809, 0.1255), (−0.0892, 0.0722, 0.1233) [48].

Table 2

Theoretical and experimental structural parameters using LDA of ternary compounds $BiGa_2X_4$ ($X = S, Se$).

Ternary compounds	
$BiGa_2S_4$	$BiGa_2Se_4$
a = 7.531 Å, Exp: (7.458 Å) [48].	a = 7.762 Å, Exp: (7.708 Å) [48].
c = 12.043 Å, Exp: (12.032 Å) [48].	c = 12.488 Å, Exp: (12.514 Å) [48].
c/a = 1.599, (1.613) [48].	c/a = 1.608, (1.624) [48].
B_0 = 70.961 GPa.	B_0 = 61.938 GPa.
B' = 4.792.	B' = 4.952.
$\Delta a/a$ $_{EXP}$ = 0.968.	$\Delta a/a$ $_{EXP}$ = 0.695.
$\Delta c/c$ $_{EXP}$ = 0.088.	$\Delta c/c$ $_{EXP}$ = −0.208.
V_0 = 682.989 Å³, (669.2 Å³) [48].	V_0 = 752.385 Å³, (743.5 Å³) [48].
E_0 = −216359.0890 Ryd.	E_0 = −281289.4850 Ryd.

Fig. 2 illustrates the energy predictions for $BiGa_2S_4$ and $BiGa_2Se_4$ as functions of the conventional cell volume. The E-V data was utilized to derive structural features via the Murnaghan state equation (EOS) [49]. Table 2 provides a summary of experimental data [48], along with the calculated lattice constants a and c, compressibility modulus B_0, and pressure derivative B'.

The calculated lattice constants are as follows: a = 7.531 Å (7.458 Å [48]) and c = 12.043 Å (12.032 Å [48])) for $BiGa_2S_4$, and a = 7.762 Å (7.708 Å [48]) and c = 12.488 Å (12.514 Å [48]) for $BiGa_2Se_4$. The deviation from the experimental values are $\Delta a/a$ $_{EXP}$ = 0.968 % and $\Delta c/c$ $_{EXP}$ = 0.0880 % [$\Delta a/a$ $_{EXP}$ = 0.6957 % and $\Delta c/c$ $_{EXP}$ = −0.2082 %] for $BiGa_2S_4$ [$BiGa_2Se_4$].

This study reports the ground state values of E_{min}, B_0, and B' for $BiGa_2S_4$ and $BiGa_2Se_4$, marking the first such report for these bismuth-based ternary compounds. $BiGa_2X_4$ ($X = S, Se$) crystallizes in the tetragonal space group $P4/nnc$, as illustrated in Fig. 1a and b. There exist two non-identical Ga sites (Fig. 1c and d). Ga (1) forms bonds with four equivalent S (Se) atoms at the first location, S (1) (Se (1)), creating GaX_4 ($X = S, Se$) tetrahedra that share edges. The bond lengths for Ga (1) -S (1) (Se (1)) are all 2.27439 Å (2.407 Å). Ga (2) bonds with four equivalent atoms S (1) (Se (1)) to form GaX_4 ($X = S, Se$) tetrahedra that share edges. The bond lengths for Ga (2) -S (1) (Se (1)) are all 2.2717 Å (2.435 Å). Bi (1) bonds with four atoms, S (1) (Se (1)), forming a distorted rectangular rocking-saw geometry. The calculated bond lengths for Bi (1) -S (1) (Se (1)) are all 2.8116 Å (2.92911 Å).

3.2. Electronic properties

The band structure of $Bi_2Al_4Se_8$ was determined through the linear muffin-tin orbital (LMTO) method, utilizing designated vectors within

Table 3

Selected interatomic distances (Å) and angles (deg) in ternary compounds $BiGa_2S_4$ and $BiGa_2Se_4$.

Compounds	Distances and angles between atoms	Our LDA-based computations	Resulting Experiments [48].
$BiGa_2S_4$	Bi–Bi (×1)	3.107 Å	3.144 Å
	Bi–S (× 4)	2.811 Å	2.842 Å
	Ga (1)-S (×4)	2.274 Å	2.294 Å
	Ga (2)-S (×4)	2.271 Å	2.287 Å
	S–Ga (1) -S (×2)	97.133°	97.7°
	S–Ga (1)-S (×4)	115.121°	115.65°
	S–Ga (2) -S (×2)	96. 983°	98.1°
	S–Ga (2) -S (×2)	115.121°	113.2°
	S–Ga (2) -S (×2)	116.826°	117.7°
$BiGa_2Se_4$	Bi–Bi (×1)	3.090 Å	3.148 Å
	Bi–Se (× 4)	2.9291 Å	2.952 Å
	Ga (1)-Se (×4)	2.407 Å	2.395 Å
	Ga (2)-Se (×4)	2.435 Å	2.402 Å
	Se–Ga (1) -Se (×2)	98.593°	100.3°
	Se–Ga (1)-Se (×4)	115.168°	114.2°
	Se–Ga (2) -Se (×2)	98. 5936°	98.7°
	Se–Ga (2) -Se (×2)	115.1689°	111.5°
	Se–Ga (2) -Se (×2)	116.3734°	118.8°

the Brillouin zone [50]. The calculated bandgap, $E_g \approx 2$ eV, closely aligns with the measured value of 1.9 eV [48]. To gain insights into the electronic structure, we analyzed the band structure, total, and partial density of states (DOS) as shown in Figs. 3 and 4. The DOS and band structure of $BiGa_2X_4$ ($X = S, Se$) compounds were computed using LDA and mBJ − LDA approximations. The band structure simulations reveal that both $BiGa_2S_4$ and $BiGa_2Se_4$ compounds are indirect gap semiconductors under both the LDA and mBJ − LDA approximations (Fig. 3).
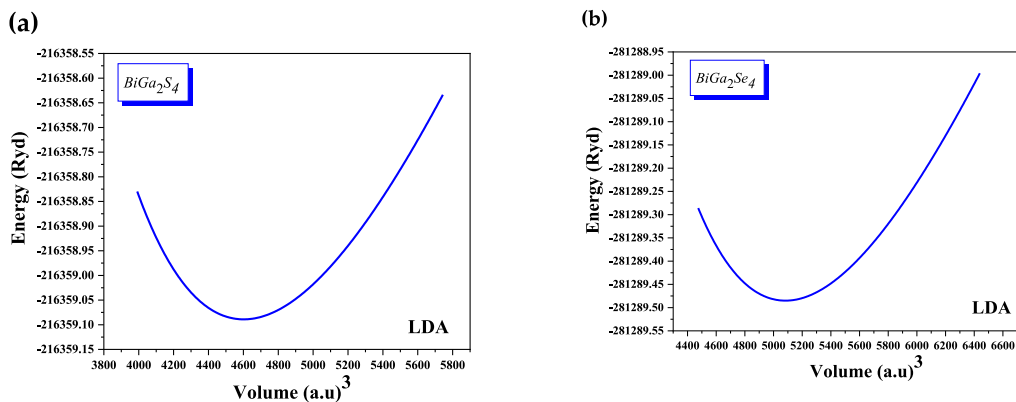

Fig. 2. Variation of the total energy E(Ry) as a function of volume for $BiGa_2X_4$ ($X = S, Se$) ternary compounds with the LDA approximation.
S (1) (Se (1)) combine in an irregular, non-coplanar trigonometric shape to create Ga(1), Ga(2), and Bi(1). The angles formed by the S (Se)-Ga (1)-S (Se) (× 2), S (Se)-Ga (1)-S (Se) (× 4) atoms are 97.1330° (× 2) (98.5936°) (× 2), 115.1218° (× 4) (115.1689°) (× 4). These values are in good agreement with the experimental results of 97.7° (100.3°), 115.65° (114.2°) [48] (Table 3).
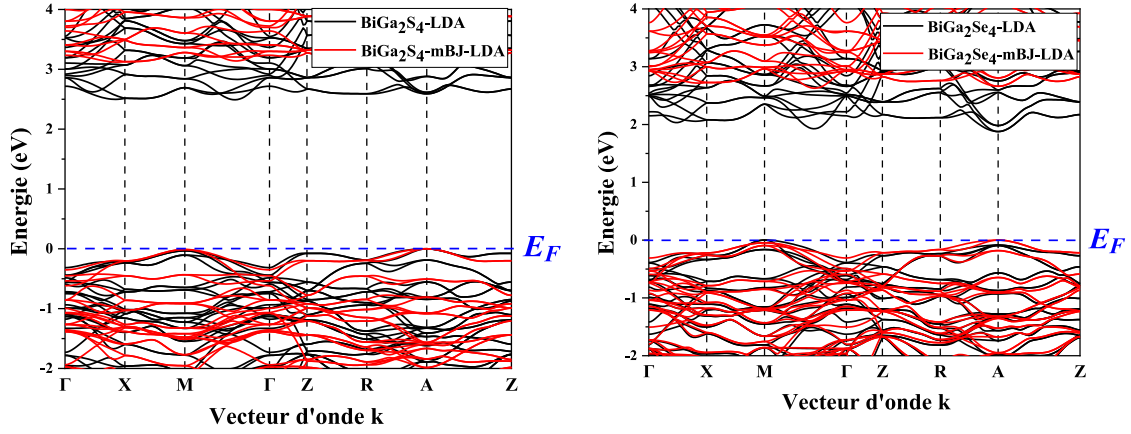
Fig. 3. Band structure along the *Brillouin zone* symmetry lines for $BiGa_2X_4$ ($X = S, Se$) compounds.
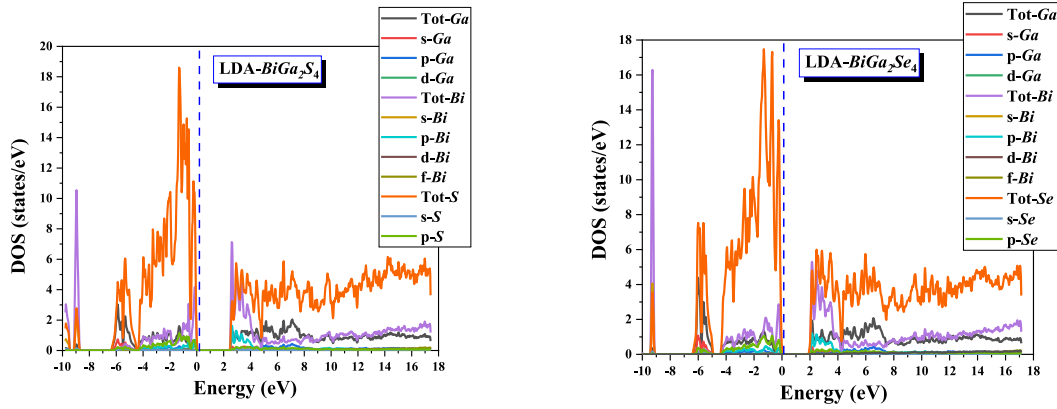

Fig. 4. Total and partial densities of states were calculated for the compounds $BiGa_2S_4$ and $BiGa_2Se_4$.

The calculated bandgaps, $E_g = 2.504$ eV and $E_g = 1.878$ eV, using the LDA approximation, are in good agreement with the experimental values of 2.1 eV and 1.8 eV for $BiGa_2S_4$ and $BiGa_2Se_4$ respectively [48] (Table 4).

These observed bandgaps correspond to an indirect transition from (A → M-Γ) and (M → A) for $BiGa_2S_4$ and $BiGa_2Se_4$, respectively, and both materials exhibit *p*-type semiconducting behavior, with the Fermi energy close to the valence band maximum (VBM). To assess the size and charge carriers' characteristics, it's essential to determine the effective mass parameter. The effective mass can be predicted based on the dispersion curves obtained for various k-values along the electronic band geometry. The effective mass is larger for flat bands compared to curved energy curves for a given k-value. In this case, the energy curve for $BiGa_2S_4$ and $BiGa_2Se_4$ exhibits flat behavior along the symmetry paths (A → M-Γ) and (M → A), suggesting significant effective mass for carriers in these directions, which indicates the potential for efficient thermoelectric properties.

In the context of $BiGa_2X_4$ ($X = S, Se$) semiconductors, holes are likely to serve as the predominant charge carriers, playing a pivotal role in the thermoelectric characteristics of these materials. The DOS (Fig. 4) highlights the dominance of *S-p* (*Se-p*) states just below the Fermi energy, with significant contributions from the 4*p*-filled orbitals of sulfur and selenium. Moreover, the empty 6*p* levels of trivalent Bi^{+3} are prevalent at around 2 eV above the Fermi energy. These $p - p$ interactions between bismuth, sulfur, and selenium p-orbitals play a significant role in determining the energy bandgap in these materials, while gallium's low-energy *s* and *p* bands make a minimal contribution to the gap.

3.3. Optical properties

The mBJ – LDA method predicts various optical characteristics within the energy range of 0–24 eV. In the tetragonal structure, we distinguish two types of polarization: extraordinary polarization (where the field is oriented along the *x* or *y* axis) and ordinary polarization (with the field directed along the *z* axis). The computed values of the

Table 4
Values of energy gap Eg (eV), $\varepsilon_1(0)$ and $n(0)$ calculated for $BiGa_2X_4$ ($X = S, Se$) semiconductors with the LDA and mBJ-LDA approaches.

Ternary compounds	$E_g(eV)$			$\varepsilon_1(0)$			$n(0)$		
	LDA	mBJ-LDA	Exp		LDA	mBJ-LDA		LDA	mBJ-LDA
$BiGa_2S_4$	2.504	3.127	2.1 [48]	ε_{1xx}	8.319	6.140	n_{xx}	2.884	2.478
				ε_{1zz}	8.100	6.074	n_{zz}	2.846	2.464
$BiGa_2Se_4$	1.878	2.654	1.8 [48]	ε_{1xx}	10.418	7.817	n_{xx}	3.227	2.796
				ε_{1zz}	9.590	7.234	n_{zz}	3.096	2.689

imaginary component $\varepsilon_2(\omega)$ of the dielectric function for $BiGa_2X_4$ ($X = S$, Se) compounds are presented in Fig. 5a.

This investigation reveals that all $BiGa_2X_4$ ($X = S$, Se) semiconductors exhibit very similar optical behavior. The first significant parameters of the dielectric function correspond to the fundamental absorption criteria, commencing at 1.972 eV for $BiGa_2S_4$ and 1.809 eV for $BiGa_2Se_4$. These values are associated with the transitions ($A \rightarrow M - \Gamma$) and ($M \rightarrow A$) for $BiGa_2S_4$ and $BiGa_2Se_4$, respectively. Adjacent to the fundamental peak, we observe principal peaks along the $x - axis$ at 4.476 eV and 3.741 eV for $BiGa_2S_4$ and $BiGa_2Se_4$, respectively. Consequently, $\varepsilon_2(\omega)$ displays a prominent peak in the ultraviolet region for all materials. Beyond this peak, $\varepsilon_2(\omega)$ decreases rapidly with increasing photon energies for both compounds.

Fig. 5b shows the change in the extinction coefficient $k(\omega)$ concerning energy for the investigated materials. The spectra exhibit remarkable similarities with only minor distinctions. The maximum values of the extinction coefficient in the spectra are observed at energies of 4.585 eV and 4.204 eV along the $x - axis$ for $BiGa_2S_4$ and $BiGa_2Se_4$, respectively. Beyond these peaks, the extinction coefficient decreases rapidly with increasing photon energies for both compounds.

The real parts $\varepsilon_1(\omega)$ of the dielectric functions are determined using the Kramers-Kronig equations [51], from the corresponding imaginary parts, as summarized in Table 4. Notably, the optical spectra in this figure are comparable with minor variations.

The zero crossing in the spectra indicates the absence of scattering, and the function approaches zero, signifying peak absorption. Along the x-axis, the main peaks $\varepsilon_1(\omega)$ resulting from the mBJ $-$ LDA calculations are positioned at 3.932 eV and 2.952 eV for $BiGa_2S_4$ and $BiGa_2Se_4$, respectively. These correspond to ultraviolet wavelengths for $BiGa_2S_4$ and the visible region for $BiGa_2Se_4$. The $\varepsilon_1(\omega)$ values become zero at energies of 7.850 eV and 4.748 eV for $BiGa_2S_4$ and $BiGa_2Se_4$, respectively. The spectra then exhibit negative values, reaching a minimum before gradually decreasing to zero again at 18.381 eV for $BiGa_2S_4$ and at 17.837 eV for $BiGa_2S_4$ and $BiGa_2Se_4$ compound displays the highest intensity peak. A slight anisotropy is observed for $BiGa_2S_4$ and $BiGa_2S_4$ compounds, with values of ($\varepsilon_{1xx}(0) = 8.319$, $\varepsilon_{1zz}(0) = 8.10$), and ($\varepsilon_{1xx}(0) = 10.418$, $\varepsilon_{1zz}(0) = 9.59$), respectively, using the LDA approximation. Furthermore, $BiGa_2Se_4$ exhibits a higher dielectric constant compared to $BiGa_2S_4$. Penn's equation, $\varepsilon_1(0) \approx 1 + \left(\frac{\hbar\omega_P}{E_g}\right)^2$ [52], where E_g represents the energy bandgap, and ω_P is the plasma frequency, can help explain this observation. In this case, the calculated E_g for $BiGa_2S_4$ is slightly larger than that for $BiGa_2Se_4$, resulting in a smaller energy bandgap and a higher value of $\varepsilon_1(0)$ in the latter.

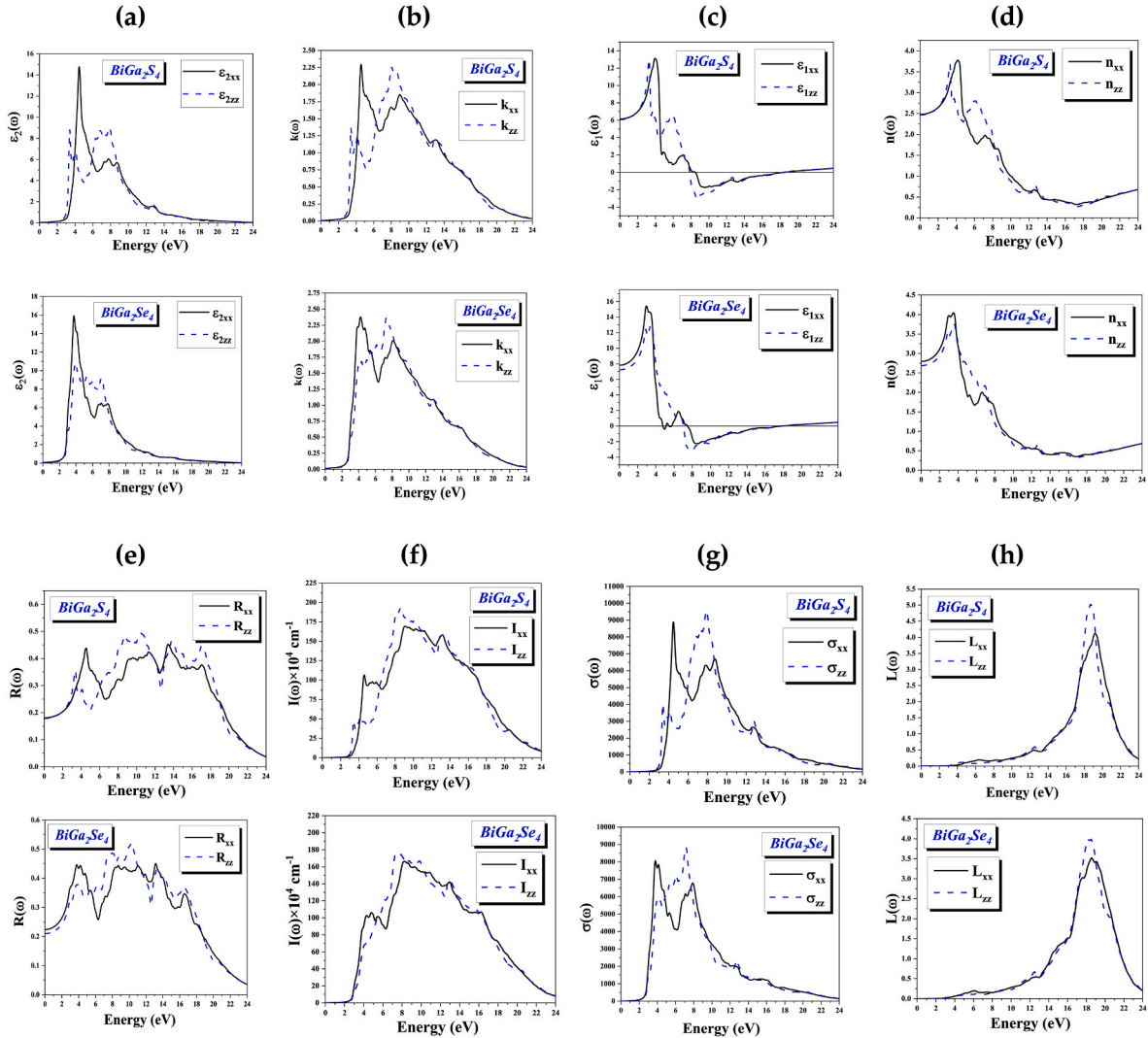The spectra are displayed in Fig. 5d, where the refractive index

Fig. 5. (a) and **(b)** Alterations to the imaginary function of dielectrics and the extinction coefficient, respectively, **(c)** real parts of the dielectric function, **(d)** the refractive index, **(e)** reflectivity spectra, **(f)** the absorption coefficient, **(g)** variations of optical conductivity, and **(h)** the energy loss function as a function of energy for $BiGa_2X_4$ ($X = S$, Se) within the mBJ-LDA approximation.

generally follows the profile of the real part, and they are linked by the equation $n(0) = \sqrt{\varepsilon_1(0)}$. In these refractive index spectra, sharp peaks at the edge of the energy bandgap are attributed to excitonic transitions. The zero-frequency refractive indices of the compounds are (n_{xx} = 2.478, n_{zz} = 2.464), and (n_{xx} = 2.796, n_{zz} = 2.689) for *BiGa$_2$S$_4$,* and *BiGa$_2$S$_4$,* as determined using the mBJ – LDA approximation. The refractive index value increases with rising photon energy up to 4 eV, after which it begins to decrease up to a photon energy of 24 eV. It also exhibits non-linear behavior. The calculated static refractive index, $n(0)$, is presented in Table 4. To the best of our knowledge, there is no available experimental data for comparison. The calculated results also reveal that both the real part and the refractive index exhibit slight anisotropy. The variation of reflectivity, as calculated by the mBJ – LDA approximation, is depicted in Fig. 5e as a function of energy for *BiGa$_2$S$_4$* and *BiGa$_2$Se$_4$.* These semiconductors exhibit low reflectivity in the low-energy region, beginning at 18.06% for *BiGa$_2$S$_4$* and 22.38% for *BiGa$_2$Se$_4$* along the z and $x-$ axes, respectively. As energy increases to intermediate and high photon energies, reflectivity rapidly increases, reaching its peak value around 10.51 eV for *BiGa$_2$S$_4$* along the $z-axis$ and 10.27 eV for *BiGa$_2$Se$_4$* along the $z-axis$. These maxima in reflectivity are a result of interband transitions. As energy continues to increase, reflectivity decreases. The absorption coefficients for *BiGa$_2$S$_4$* and *BiGa$_2$Se$_4$* semiconductors, calculated using the mBJ – LDA approximation, are presented in Fig. 5f. Notably, a significant increase in the absorption coefficient is observed in the low-energy region, with the highest value reached at the highest energy. For *BiGa$_2$S$_4$,* a strong peak is observed at 8.61 eV along the z-axis. The absorption spectra show maxima in the energy range of $6.65 - 16.55$ eV. In the case of *BiGa$_2$Se$_4$,* a strong peak is observed at 7.33 eV along the $z-axis$, and the absorption spectra show maxima in the energy range of $5.94 - 14.89$ eV. Consequently, the highest absorption peaks occur in the ultraviolet region for both compounds. These peaks are attributed to interband transitions in the electronic band spectrum between various high-symmetry points. In addition, the absorption along the $z-axis$ ($E \parallel c$) is higher than that along the $x-$ and $y-axes$ ($E \perp c$), resulting in higher main peaks for I_{zz} compared to I_{xx}. Furthermore, these compounds exhibit significant UV absorption characteristics, as shown in Fig. 5f.

Comparison reveals that the reported bandgaps for *CuBiS$_2$, Cu$_3$BiS$_3$,* and *Cu$_4$Bi$_4$S$_9$* fall within the range of 1.5–2.62 eV, 1.2–1.84 eV, and 0.88–1.14 eV, respectively, which are suitable for photovoltaic applications and fall within the range of 1.3–1.7 eV in their bulk forms. In contrast, the electron voltage bandgap for *BiGa$_2$S$_4$* and *BiGaSe$_4$* compounds is approximately 2.504 eV and 1.878 eV, respectively, in excellent agreement with the corresponding values calculated using the LDA approximation. The reported absorption coefficients for *CuBiS$_2$, Cu$_3$BiS$_3$,* and *Cu$_4$Bi$_4$S$_9$* are in the range of 10^4–10^5 cm^{-1}. The calculated absorption coefficients for *BiGa$_2$S$_4$* and *BiGaSe$_4$* are within the range of 0.6839×10^5 to 0.9156×10^5 cm^{-1} for zz and xx, and 0.7333×10^5 to 0.8258×10^5 cm^{-1} for zz and xx, respectively.

The optical conductivity, denoted by $\sigma(\omega)$, signifies the connection between the oscillating electric field $E(\omega)$ and the current density $j(\omega)$ [53]. For $\omega \to 0$, the real component of $\sigma(\omega) = \frac{\omega}{4\pi}\varepsilon_2$ is directly linked to its imaginary component. Fig. 5g illustrates the optical conductivity spectrum, revealing numerous peaks corresponding to transitions between bands. Sharp edges are observed in the UV region within the energy range of $4 - 9$ eV, as previously discussed [54,55].

The energy loss function can be derived from the dielectric function, as suggested in prior work. Energy loss spectra for *BiGa$_2$S$_4$* exhibit substantial values in the energy range from 17.51 to 20.17 eV, with a sharp peak along the $z-axis$ at 18.65 eV *BiGa$_2$Se$_4$* also displays significant energy loss in the energy range of 16.88–20.39 eV, with the largest peak along the z-axis at 18.49 eV. The primary peak for both *BiGa$_2$S$_4$* and *BiGa$_2$Se$_4$* semiconductors occurs when $\varepsilon_2(\omega)$ is minimal, and $\varepsilon_1(\omega)$ returns to zero. The average peak of the energy loss function corresponds to the plasma frequency ω_p. For instance, the plasma energy ω_p peaks at

18.65 eV for *BiGa$_2$S$_4$* and 18.49 eV for *BiGa$_2$Se$_4$*, as shown in Fig. 5h.

3.4. Elastic properties

Elastic constants, denoted as C_{ij}, govern the elasticity of a crystal and its response to externally applied forces. In the case of tetragonal structures, six distinct elastic constants are considered: C_{11}, C_{12}, C_{13}, C_{33}, C_{44}, and C_{66}. Accurate estimations of these elastic constants require an understanding of how energy changes with strain for various deformations. Specifically, deformations that optimize the symmetry of strained systems [56] are selected. The WIEN2K package offers a useful feature for the force-driven optimization of the internal cell shape to facilitate this process. In this study, the LDA approximation was employed to determine the elastic characteristics of *BiGa$_2$S$_4$* and *BiGa$_2$Se$_4$* semiconductors, and the resulting elastic moduli are presented in Table 5.

It is important to note that these elastic constants must satisfy specific criteria for the structures to be considered mechanically stable.

$$\begin{cases} C_{11} > 0, C_{33} > 0, C_{44} > 0, C_{66} > 0, C_{11} > |C_{12}|, \\ \qquad\qquad C_{11}C_{33} > C_{13}^2 \\ \qquad (C_{11} + C_{12})C_{33} > 2C_{13}^2 \end{cases} \qquad (1)$$

Based on the criteria established, both compounds meet the requirements for mechanical stability. This is evident as all six independent elastic constants are positive, signifying the stability of both *BiGa$_2$S$_4$* and *BiGa$_2$Se$_4$* (Table 5). The elastic constants follow the sequence: C_{ij} (*BiGa$_2$S$_4$*) > C_{ij} (*BiGa$_2$Se$_4$*), with $C_{33} > C_{11}$, indicating that the a-axis of each compound is slightly more compressible than the c-axis. Furthermore, it suggests that shearing in the (001) plane is easier than shearing in the (100) plane, given that C_{44} is smaller than C_{66}. Leveraging the obtained elastic constants, we were able to derive a range of mechanical parameters, including the bulk modulus (B), shear modulus (G), Poisson's ratio, and anisotropy factors. In Table 6, we have presented the Voigt (V), Reuss (R), and Hill (H) approximations. The bulk modulus quantifies a material's resistance to volume change while retaining its shape [57]. It is noteworthy that the bulk modulus for these materials follows the order: B_H (*BiGa$_2$S$_4$*) > B_H (*BiGa$_2$Se$_4$*). The bulk modulus values were calculated using the elastic constants according to the Voigt – Reuss – Hill model [58–60] and they agree with the estimates obtained from total energy minimization for each material (Table 2).

In the context of materials, the shear modulus, which quantifies their resistance to deformation, holds greater significance than hardness [57]. A higher shear modulus is primarily attributed to the presence of a larger C_{44}. The mechanical properties of materials are commonly classified as brittle or ductile [61]. Generally, brittleness is observed when the B/G ratio falls below 1.75. Materials become brittle when this ratio is less than 1.75, whereas they exhibit ductility when the ratio surpasses this value. Based on the data presented in Table 6, both compounds are categorized as brittle, as their calculated B/G ratio is less than 1.75. Poisson's ratio (σ) offers insight into the nature of the forces that bind atoms in a material. For solids, the Poisson's ratio ranges between 0.25

Table 5
Elastic constants of *BiGa$_2$S$_4$* and *BiGa$_2$Se$_4$* within the LDA approach.

Compounds	*BiGa$_2$S$_4$*	*BiGa$_2$Se$_4$*
C_{11}	109.5624	96.6538
C_{12}	51.6163	47.9594
C_{13}	43.2041	38.2318
C_{33}	145.2441	120.9631
C_{44}	53.4176	46.9683
C_{66}	63.0951	59.2661
T_m	900.553 ± 300	825.406 ± 300
A_1	1.26884	1.33099
A_2	2.17772	2.43421

Table 6
Modules of elasticity of *BiGa₂S₄* and *BiGa₂Se₄* utilizing the LDA estimation.

Compounds	$BiGa_2S_4$	$BiGa_2Se_4$
B_V	71.157	62.568
B_R	70.564	62.366
B_H	70.860	62.467
G_V	49.075	43.296
G_R	45.661	39.590
G_H	47.368	41.443
E_V	119.705	105.543
E_R	112.678	98.027
E_H	116.209	101.813
σ_V	0.219	0.218
σ_R	0.233	0.238
σ_H	0.226	0.228
B_H/G_H	1.49596	1.50729
A_B	0.41815	0.161892
A_G	3.60428	4.47234
A^u	0.382302	0.471416

(lower bound) and 0.50 (upper bound) [62]. In the cases of both *BiGa₂S₄* and *BiGa₂Se₄*, their Poisson's ratios are less than 0.25, suggesting that the forces at play are not perfectly centered or that the chemical bonds may be hybrid combinations of ionic and covalent types. Shear anisotropy is another critical aspect, as it signifies the level of elastic anisotropy present in a material. The results of our calculations are presented in Table 5. For tetragonal structures, the following equations are employed to compute the shear anisotropy factors A₁ in the {100} plane and A₂ in the {001} plane [56,62,63]:

$$A_1 = 4C_{44} / (C_{11} + C_{33} - 2C_{13}) \quad (2)$$

$$A_2 = 2C_{66} / (C_{11} - C_{12}) \quad (3)$$

The anisotropy factors presented in Table 5 reveal that both *BiGa₂S₄* and *BiGa₂Se₄* exhibit anisotropy along both the 100 and 001 crystallographic directions. Notably, the c-axis shear anisotropy is significantly more pronounced than that along the a-axis in both compounds. It is also evident that *BiGa₂Se₄* has a higher anisotropy factor compared to *BiGa₂S₄*. In addition, we conducted calculations to determine the elastic anisotropy of these crystalline materials, which we denoted as $A_B = (B_V - B_R)/(B_V + B_R) \times 100$ for compressibility and $A_G = (G_V - G_R)/(G_V + G_R) \times 100$ for shear [63–65]. The results displayed in Table 6 indicate that *BiGa₂S₄* and *BiGa₂Se₄* have A_B % (A_G%) values of approximately 0.41815 (3.60428) and 0.161892 (4.47234), respectively. These values suggest a moderate degree of isotropy in compressibility and a high level of elastic anisotropy in shear. In this context, 0 % represents elastic isotropy, while 100 % signifies the greatest elastic anisotropy. It is important to note that BiGa₂S₄ exhibits a higher (lower) compressibility anisotropy in shear compared to *BiGa₂Se₄*.

Another essential factor in elastic anisotropy analysis is the universal anisotropy index (A^U) [66], determined by the equation $A^U = 5\frac{G_V}{G_R} + \frac{B_V}{B_R} - 6$. When $A^U = 0$, it signifies elastic isotropy, whereas $A^U \neq 0$ indicates elastic anisotropy.

In the analysis, all tested functions indicate the presence of elastic anisotropy in both compounds. However, while informative, the above analysis may not be sufficient for the precise determination of a crystal's elastic properties. In practical terms, surface structures should consider linear compressibility and the reciprocal of Young's modulus with various orientations. The linear compressibility in tetragonal systems is described as:

$$\beta = (S_{11} + S_{12} + S_{13}) - n^2(S_{11} + S_{12} - S_{13} - S_{33}) \quad (4)$$

Here, n represents the unit vector's direction, with $n^2 = 0$ for n⊥c and $n^2 = 1$ for n//c.

In tetragonal systems, the reciprocal of Young's modulus E in the

direction of the unit vector n_i is expressed as [67],

$$E = \frac{1}{S_{11} - (S_{11} - S_{33})n_3^4 - 2(S_{11} - S_{13})(n_1^2 n_3^2 + n_2^2 n_3^2) - (2S_{11} - 2S_{12} - S_{66})n_1^2 n_2^2} \quad (5)$$

In spherical coordinates, the directions along the x, y, and z axes correspond to the cosines $n_1 = \sin\theta\cos\phi$, $n_2 = \sin\theta\sin\phi$, and $n_3 = \cos\theta$, where S_{ij} is the deformability elastic constant. Utilizing the computational elastic coefficients shown in Fig. 6a-d, we can calculate the linear compressibility of BiGa₂S₄ and BiGa₂Se₄ compounds. The linear compressibility's isotropic nature results in a spherical representation of the cubic system, highlighting the isotropic character of linear compressibility in Fig. 6a-d.

For the *BiGa₂X₄ (X = S, Se)* semiconductors, elasticity anisotropy in the (XZ) and (YZ) planes is more pronounced than in the (XY) plane, where the compressibility modulus appears isotropic when considering the (X = Y) plane. The orientation-dependent Young's modulus for *BiGa₂S₄* and *BiGa₂Se₄* is illustrated in Fig. 6(e–h) using elastic compliance coefficients as a reference. The solution to Equation (5) creates a 3D
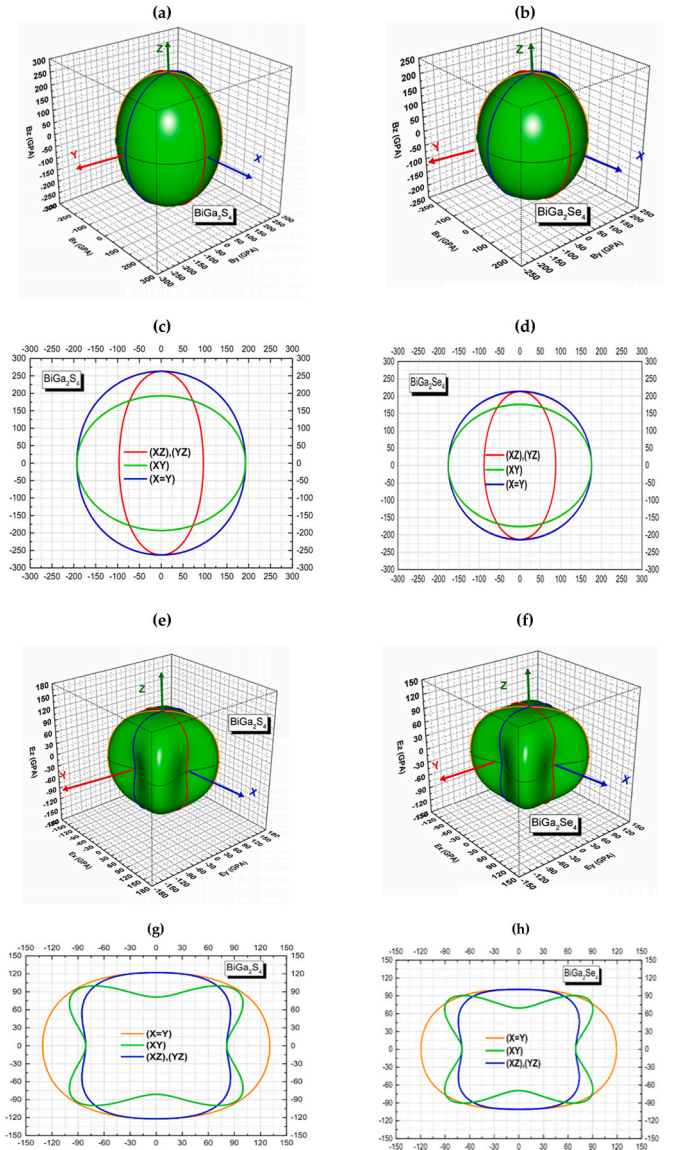

Fig. 6. Graphs of 3D surface of (a) and (b) the compressibility modulus, (e) and (f) the Young's modulus for *BiGa₂S₄*, *BiGa₂Se₄*, respectively, and (c), (d), (g), and (h) their transverse sections in separated planes.

closed surface, and the distance between the origin of the coordinate system and this surface corresponds to Young's modulus in the specified direction. If the system were entirely isotropic, this surface would have a spherical shape. However, it's evident that the Young's modulus surfaces of $BiGa_2S_4$ and $BiGa_2Se_4$ are not spherical, demonstrating a high level of anisotropy due to varying bonding properties between neighboring atomic planes, resulting in larger interplane distances. Anisotropy is more significant in the (XY) plane for $BiGa_2X_4$ (X = S, Se) materials than in the (XZ) and (YZ) planes, and both compounds are practically isotropic in the plane where X and Y are equal.

The Debye temperature (θ_D) and average, transverse, and longitudinal sound velocities can be determined using the formulas [68–70]. The calculated values for average, transverse, and longitudinal sound velocities, as well as the θ_D for the compounds under investigation are summarized in Table 7.

Under standard conditions and using the LDA approximation, the values of θ_D for $BiGa_2S_4$ and $BiGa_2Se_4$ are 363.332 K and 292.63 K, respectively. It's worth noting that the velocity of elastic longitudinal waves is higher than that of elastic transverse waves. When the θ_D is low, and the Grüneisen parameter is high, a material's lattice thermal conductivity decreases due to increased anharmonicity. Consequently, this leads to a high figure of merit (ZT).

3.5. Thermoelectric properties

Utilizing the BoltzTrap2 program, we applied the rigid band approach to solve the Boltzmann formula. In $n - type$ ($p - type$) semiconductors, the Fermi level nears the conduction (valence) band, and when doping concentration is low, the rigid band model remains valid [71]. Thus, we exclusively examine the pristine unit cell structure of the material. Fig. 7a and b depict the thermal conductivity components, k_L and k_e, which collectively constitute the overall thermal conductivity, k_T. Various methods can be employed to determine the k_L parameter [72,73]. For Slack's method, Morelli demonstrated that bulk and shear modulus could be used to ascertain the intrinsic k_L of a material [72,73]. The electronic thermal conductivities (k_e) of the two semiconductors under investigation were calculated using the BoltzTrap program.

Inspection of Fig. 7a reveals that k_L of the $BiGa_2S_4$ semiconductor decreases as a function of temperature, while for the $BiGa_2Se_4$ semiconductor, the trend is reversed for temperatures exceeding 400 K. The k_L values for $BiGa_2S_4$ and $BiGa_2Se_4$ at 300 K are 1.57 W/ mK and 1.14 W/ mK, respectively. At 1000 K, the k_L value for $BiGa_2S_4$ is 0.36 W/ mK, and for $BiGa_2Se_4$, it is 4.90 W/mK. Fig. 7a demonstrates that, in comparison to $BiGa_2Se_4$, the k_L of $BiGa_2S_4$ is higher; however, this trend reverses when the temperature exceeds 400 K. Consequently, the compound $BiGa_2Se_4$ exhibits the highest phonon-phonon interaction strength when the temperature is below 400 K, but when T exceeds 400 K, $BiGa_2S_4$ displays the highest phonon-phonon interaction strength. This result suggests that both semiconductors are promising candidates for superior thermoelectric performance due to their low k_L values. When tested at room temperature, the Gruneisen values of $BiGa_2X_4$ (X = S, Se) are as follows: γ ($BiGa_2S_4$) = 2.2298 and γ ($BiGa_2Se_4$) = 2.3098. $BiGa_2X_4$ (X = S, Se) exhibits a significant degree of inharmonicity owing to their considerable γ values and low k_L in their structure. Conversely, temperature leads to an increase in electronic thermal conductivity (k_e), as shown in Fig. 7b.

As shown in Fig. 7c, k_T exhibits a tendency to decrease with increasing temperature up to T = 400 K. The values of approximately 1.4710 W/m·K and 1.0101 W/m·K for $BiGa_2S_4$ and $BiGa_2Se_4$,

respectively, at 400 K affirm the relatively low thermal conductivity. The BoltzTraP program employs Boltzmann's transport theory to assess the transport characteristics of $BiGa_2S_4$ and $BiGa_2Se_4$ semiconductors [47,74]. The relaxation time (τ) is a constant, set at around 1×10^{-14} s [75–77]. σ, k_e and S may all be determined with this method [78,79]. The electronic band structure of semiconductors exerts an influence on the value of their S values. An analysis is conducted to determine whether the material can generate a voltage response to changes in temperature. The investigation has revealed that S in both $BiGa_2S_4$ and $BiGa_2Se_4$ semiconductors exhibits a diminishing trend with increasing temperature. Fig. 7d illustrates that S for $BiGa_2S_4$, and $BiGa_2Se_4$ decreases from 630.5726 μV/K and 543.4864 μV/K at 300 K to 289.4819 μV/K and 307.8122 μV/K at 1000 K. This observation implies that S maintains a consistently positive value across the entire temperature range for both $BiGa_2S_4$, and $BiGa_2Se_4$ compounds. In the context of $BiGa_2X_4$ (X = S, Se) semiconductors, it is likely that holes are the primary charge carriers, playing a pivotal role in conduction due to the positive values of S. Since the S remains positive over a broad temperature range for both $BiGa_2S_4$, and $BiGa_2Se_4$, they are categorized as $p - type$ compounds. For a more profound understanding of the semiconducting nature of these two compounds, we calculate the electrical conductivity (σ/τ) scaled by the relaxation time, as depicted in Fig. 7e. The data reveals that for $BiGa_2X_4$ (X = S, Se), (σ/τ) remains relatively constant until around 300 K, after which it gradually begins to rise, appearing to exhibit a linear relationship with temperature. At T = 300 K, the measured values for (σ/τ) are 0.0596×10^{18} ($\Omega \bullet ms$)$^{-1}$ for $BiGa_2S_4$ and 0.0755×10^{18} ($\Omega \bullet ms$)$^{-1}$ for $BiGa_2Se_4$. In particular, the observed value for $BiGa_2S_4$ at 1000 K is 6.2996×10^{18} ($\Omega \bullet ms$)$^{-1}$, while that of $BiGa_2Se_4$ is found to be 4.5183×10^{18} ($\Omega \bullet ms$)$^{-1}$.

Both $BiGa_2S_4$ and $BiGa_2Se_4$ exhibit ZT behaviors that correlate with electrical conductivity. Fig. 7f illustrates that ZT remains constant up to T = 250 K and then increases with rising temperature. Consequently, the ZT values of $BiGa_2X_4$ (X = S, Se) compounds elevate as the temperature increases. The ZT values of both $BiGa_2S_4$ and $BiGa_2Se_4$ display a notable increase, progressing from 0.6362 to 0.6996 at T = 600 K to 0.8389 and 0.8722 at T = 1000 K, respectively. In Fig. 8, we assess σ/τ, k_e/τ, S, and ZT as functions of charge carrier concentration, ranging from -3×10^{22} cm^3 to 8×10^{22} cm^3 at temperatures of 300 K, 600 K, and 900 K, respectively. Fig. 8a reveals that the (σ/τ) ratio of $BiGa_2S_4$ and $BiGa_2Se_4$ semiconductors at 300 K, 600 K, and 900 K varies with charge carrier concentration. A higher concentration of holes (electrons) results in an increased (σ/τ) ratio, while a lower concentration leads to a decreased ratio. The graphs of (σ/τ) at different temperatures clearly indicate that σ is temperature independent. This observation underscores that its behavior is governed not by the material's temperature but rather by the density of states or the transport distributions within the solid. Notably, the conduction band delocalization in $BiGa_2X_4$ (X = S, Se) compounds appears to be more substantial than the valence band delocalization around the *Fermi* level [80], as evidenced by the smaller (σ/τ) values in n-type compounds compared to $p - type$ compounds.

Fig. 8b illustrates that the ratio of k_e/τ of $BiGa_2X_4$ (X = S, Se) increases as the concentration of charge carriers rises due to the elevation of hole doping levels. Conversely, as the concentration of electron carriers' increases, (k_e/τ) decreases. Notably, k_e is influenced by temperature, whereas σ remains temperature independent. Seebeck coefficients are primarily affected by temperature at higher concentrations, resulting in a decrease as temperature rises. In Fig. 8c, it's evident that the absolute values of S for $p - type$ semiconductors surpass those of $n - type$ semiconductors. As temperature rises, the highest absolute values of S decrease and align with regions of greater carrier concentration. The changes observed in ZT curves, concerning temperature and carrier concentration, are depicted in Fig. 8d. These variations reveal that our compounds exhibit the characteristics of high-temperature thermoelectric semiconductors. Notably, the ZT values of $p - type$ semiconductors significantly exceed those of $n - type$ semiconductors. At T

Table 7
V_t, V_l, V_m, and θ_D for $BiGa_2S_4$ and $BiGa_2Se_4$ within the LDA approach.

Compounds	V_t	V_l	V_m	θ_D
$BiGa_2S_4$	3196.51 m/s	5376.67 m/s	3539.24 m/s	363.332 K
$BiGa_2Se_4$	2658.38 m/s	4480.48 m/s	2943.97 m/s	292.63 K

(a)

(b)

(c)

(d)

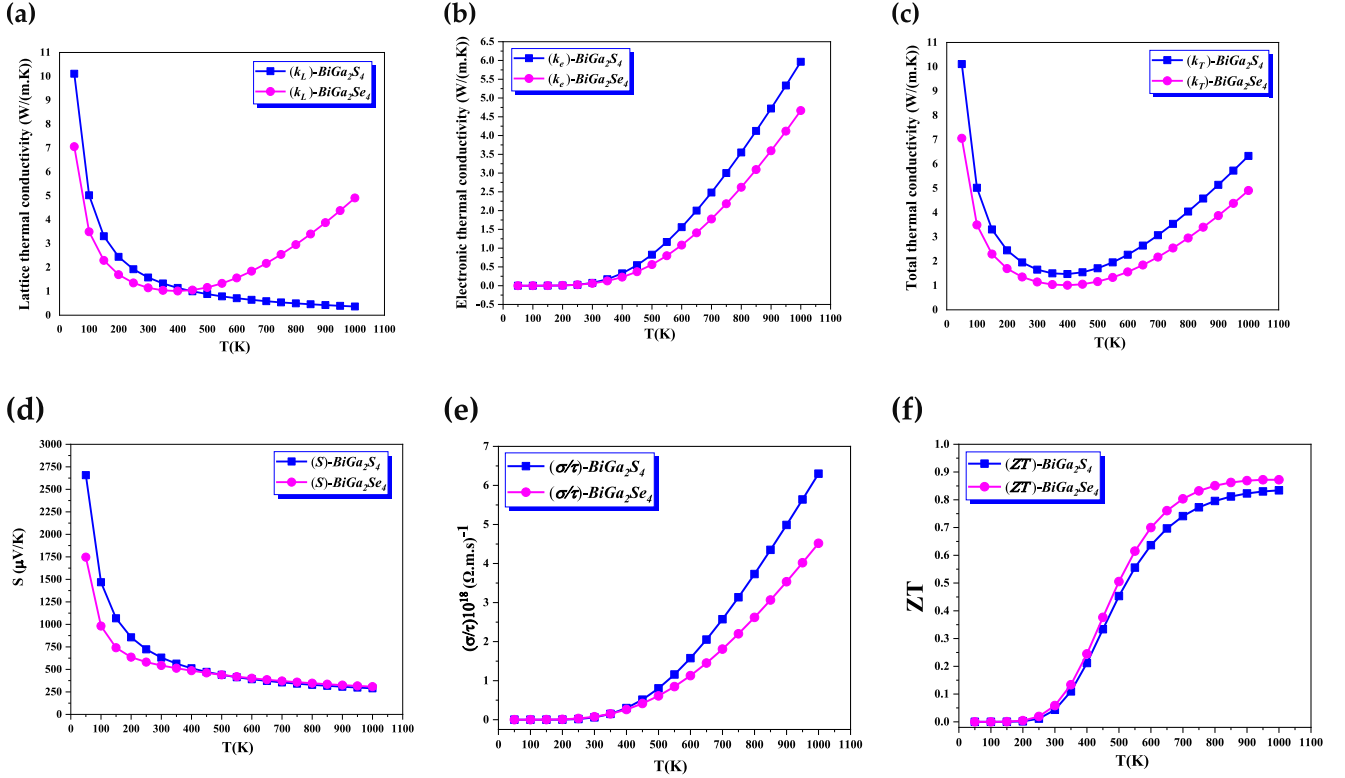**(e)**

(f)

Fig. 7. Temperature sensitivity of: the thermal conductivity of **(a)** the lattice k_L, (b) electronics k_e, (c) the total k_{Tot}, (d) Seebeck coefficients S, (e) the electrical conductivity via relaxation time (σ/τ), **(f)** the figure of merit ZT of $BiGa_2X_4$ $(X = S, Se)$ semiconductors based on the mBJ-LDA estimation.

$= 900$ K, the $p-type$ compound $BiGa_2S_4$ achieves a maximum ZT value of 0.8291 with a carrier concentration of 11.5565×10^{20} cm^3.

The $p-type$ compound $BiGa_2Se_4$ achieves an exceptional maximum ZT value of 0.9054, characterized by a carrier concentration of 8.11×10^{20} cm^3. These compelling findings underscore the substantial potential of the two compounds under scrutiny for application in the field of thermoelectric materials. For comparative analysis, the n-type-$Bi_2Al_4Se_8$ demonstrates a ZT of 0.76 at $n = -6.448 \times 10^{18}$ cm^3 [81]. Additionally, we observe variations in ZT values for other materials, such as ($CuPN_2$: $n = -1.7 \times 10^{19}$ cm^3) for $n-type$, (HPN_2: $n = 1.4 \times 10^{19}$ cm^3) for $LiPN_2$ or $NaPN_2$ ($n = 0.4 \times 10^{19}$ cm^3) for $p-type$ [82,83]. At 700 K, $CaZn_2Sb_2$ showcases a ZT value of 0.33 [84]. The $n-type$ materials $LiCrZ$ ($Z = S$, Se, Te) exhibit ZT values of 0.68, 0.9495, and 0.9507, respectively [85]. In the case of $CoFeTiGe$ ($CoFeCrGe$), ZT is documented as 0.25 and 0.404 (0.243 and 0.644) for n and $p-types$, respectively [86]. Maximum ZT readings in the spin-down direction are as follows: 0.81355 for $RbCrS$, 0.62249 for $RbCrSe$, and 1.02846 for $RbCrTe$ [87]. Following the exhibition of exceptional thermoelectric efficiency in $BiGa_2X_4$ ($X = S, Se$), we utilize the $mBJ-LDA$ method to perform comprehensive calculations of (S, σ, k_e) along both the x and z directions.

The tensors $(\sigma_{xx} = \sigma_{yy} \neq \sigma_{zz})$, $(S_{xx} = S_{yy} \neq S_{zz})$, $(k_{e_{xx}} = k_{e_{yy}} \neq k_{e_{zz}})$ all exhibit diagonal orientations. In Fig. 9a, it is observed that for the $BiGa_2S_4$ compound, the S_{xx} Seebeck coefficient parameters are slightly lower than the S_{zz} parameters, while for the $BiGa_2Se_4$ compound, the values of S_{xx} Seebeck coefficient are higher. At T $= 300$ K, the Seebeck coefficients of $BiGa_2S_4$ and $BiGa_2Se_4$ are ($S_{xx} = 621.9488$ μVK^{-1}, $S_{zz} = 647.820$ μVK^{-1}) and ($S_{xx} = 580.51061$ μVK^{-1}, $S_{zz} = 469.43803$ μVK^{-1}), respectively. This indicates that transport along the zz $(xx) - axis$ dominates for $BiGa_2S_4$ ($BiGa_2Se_4$), as evidenced by the significantly larger value of S_{zz} (S_{xx}). The (σ_{xx}) accounts for 78.37 % (61.59 %) of that at high temperatures for the semiconductor $BiGa_2S_4$ ($BiGa_2Se_4$), as indicated by the substantial density of states (DOS) related to this orientation (Fig. 9b).

As the temperature varies between 50 K and 350 K (50 K and 200 K), the electrical conductivity along the $xx - axis$ is approximately equal to the electrical conductivity along the $zz - axis$ for $BiGa_2S_4$ ($BiGa_2Se_4$). However, at elevated temperatures, the difference between these two factors becomes more pronounced. Between 50 K and 300 K (50 K and 150 K), $BiGa_2S_4$ ($BiGa_2Se_4$) exhibits electronic thermal conductivity along the xx axis that is on par with its electronic thermal conductivity along the zz axis. At higher temperatures, the contrast between these two values becomes more prominent, and ($k_{e_{zz}}$) surpasses ($k_{e_{xx}}$), with ($k_{e_{xx}}$) being determined to be 84.4901 % (94.6605 %) of that of $k_{e_{zz}}$ (Fig. 9c).

Fig. 10a and c shows the variations in ZT for $BiGa_2X_4$ ($X = S, Se$) over a broad temperature range spanning from 50 K to 1000 K. At 900 K, the ZT for $BiGa_2S_4$ reaches 0.8228, while that for $BiGa_2Se_4$ is 0.8690. These values correspond to carrier concentrations of $n_0 = 2.8399 \times 10^{20}$ cm^{-3} and 1.4645×10^{20} cm^{-3}. Both $BiGa_2S_4$ and $BiGa_2Se_4$ exhibit three distinct ZT peaks, with one peak for the $n-type$ and two peaks for the p-type, as depicted in Fig. 10b and d. Specifically, at 900 K, $BiGa_2S_4$ achieves an $n-type$ ZT maximum of 0.8289 and a $p-type$ ZT maximum of 0.5073 (Fig. 10b), while the corresponding values for the $BiGa_2Se_4$ semiconductor are 0.9053 and 0.6359 (Fig. 10d). This highlights the marked difference in the thermoelectric properties of $p-$ and $n-type$ materials. Consequently, the $n-type$ compound exhibits superior thermoelectric efficiency compared to the two semiconductors under investigation.

Furthermore, when $\mu - \mu_0 = 0$, the ZT values for $BiGa_2S_4$ and $BiGa_2Se_4$ stand at 0.6280 and 0.5793, respectively. This observation indicates that the thermoelectric performance of both compounds is enhanced even in the absence of doping. To achieve the highest attainable ZT value, it is crucial to determine the optimal carrier concentration and temperature. Further investigation into the impact of doping levels on ZT at 900 K is recommended to gain a more comprehensive understanding of the thermoelectric properties of
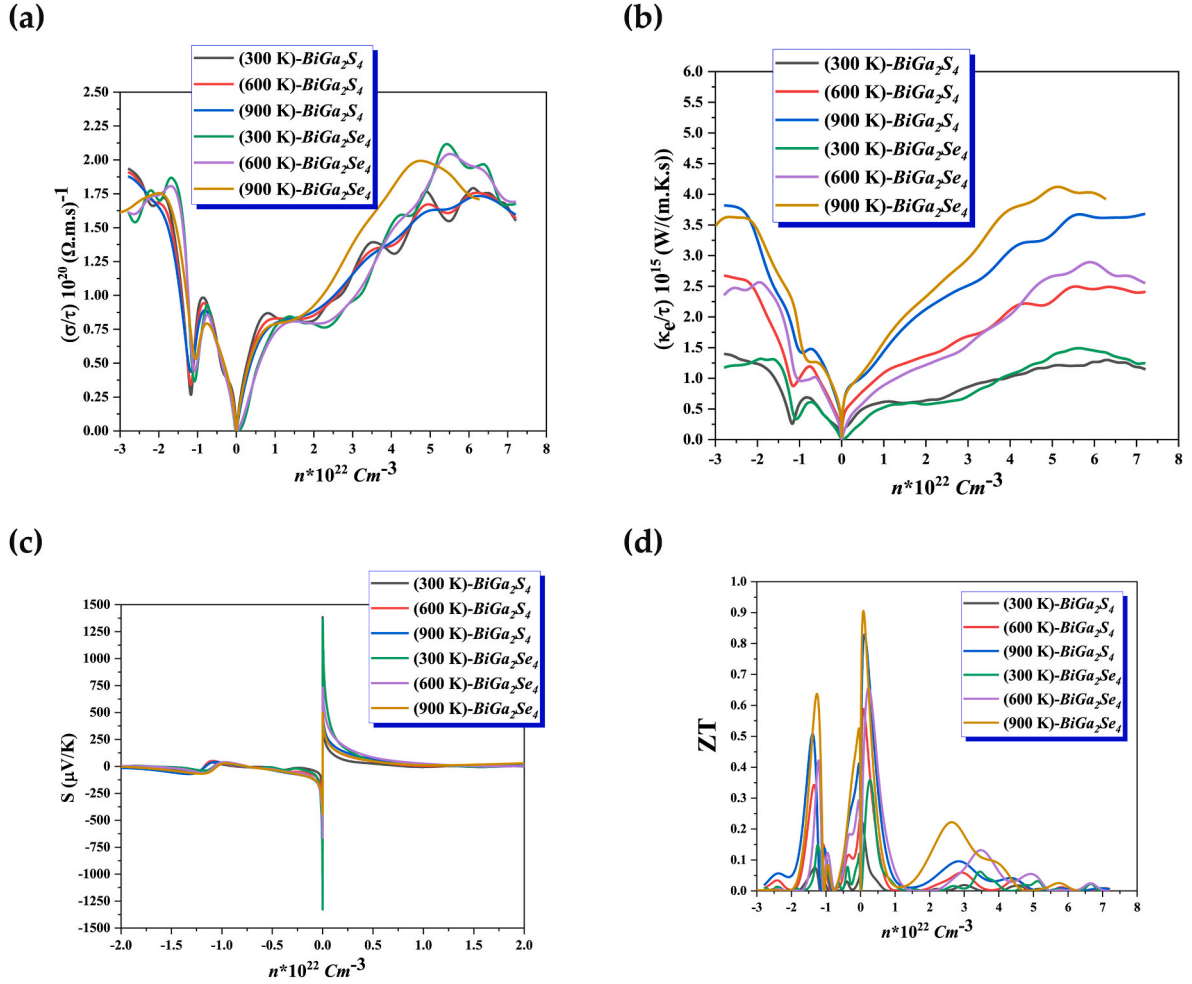
(a)

(b)

(c)

(d)

Fig. 8. Forecasted (a), (b) conductivities (electrical (σ/τ), electronic thermal (k_e/τ) as a function of relaxation time, (c) coefficient *S* of Seebeck, and (d) figure of merit *ZT* via concentrations of charge carriers when T = 300, 600, and 900 K according to the mBJ-LDA approach of *BiGa₂X₄ (X = S, Se)*.
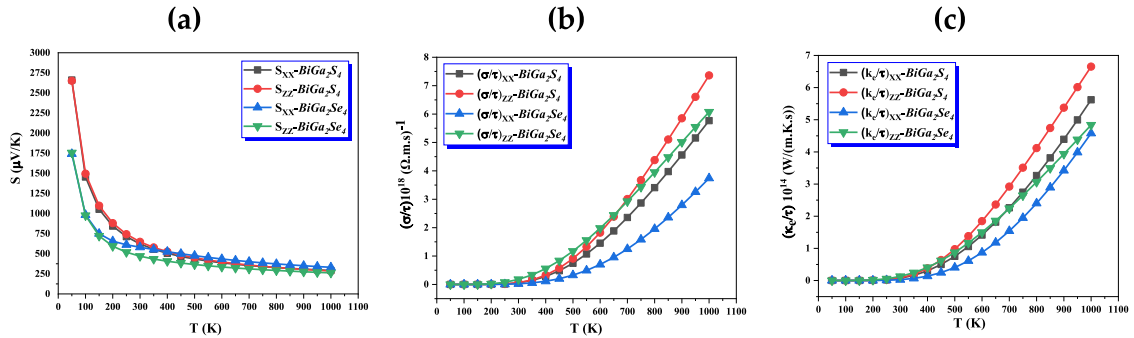
(a)

(b)

(c)

Fig. 9. Predicted anisotropic transport of *BiGa₂X₄ (X = S, Se)* **(a)** The coefficient tensor of Seebeck **(b)** The (σ/τ), tensor parts as a function of the electrical conductivity-relaxation time ratio, **(c)** The (k_e/τ) tensor parts as a function of the electronic thermal conductivity -relaxation time ratio.

semiconductors derived from *BiGa₂S₄* and *BiGa₂Se₄*. As demonstrated in Fig. 10e and g, the maximum ZT values for BiGa₂S₄ and *BiGa₂Se₄* are found to be 0.82909 and 0.90548, respectively. To achieve these values, it is necessary to increase the concentration of charge carriers to $n = 0.11715 \times 10^{22}\ cm^{-3}$ for *BiGa₂S₄* and $n = 0.0812 \times 10^{22}\ cm^{-3}$ for *BiGa₂Se₄*. The chemical potentials of the *BiGa₂S₄* and *BiGa₂Se₄* semiconductors were both reduced by 0.40151 Ry and 0.38001 Ry, respectively, yielding consistent results, as depicted in Fig. 10f and h.

4. Conclusions

Extensive research employing the FP-LAPW approach is conducted on *BiGa₂X₄ (X = S, Se)* compounds with a focus on their structural, electronic, optical, elastic, and thermoelectric aspects. The approximated structural parameters, including (*a*, *c*, *c/a*), and atomic sites, are shown to be congruent with the experimental data. The measured gaps are indirect from (A → M-Γ) and (M → A) for *BiGa₂S₄* and *BiGa₂Se₄*, respectively, with $E_g = 2.504$ eV and $E_g = 1.878$ eV using the LDA approximation. These materials' energy gap is mostly due to bismuth-
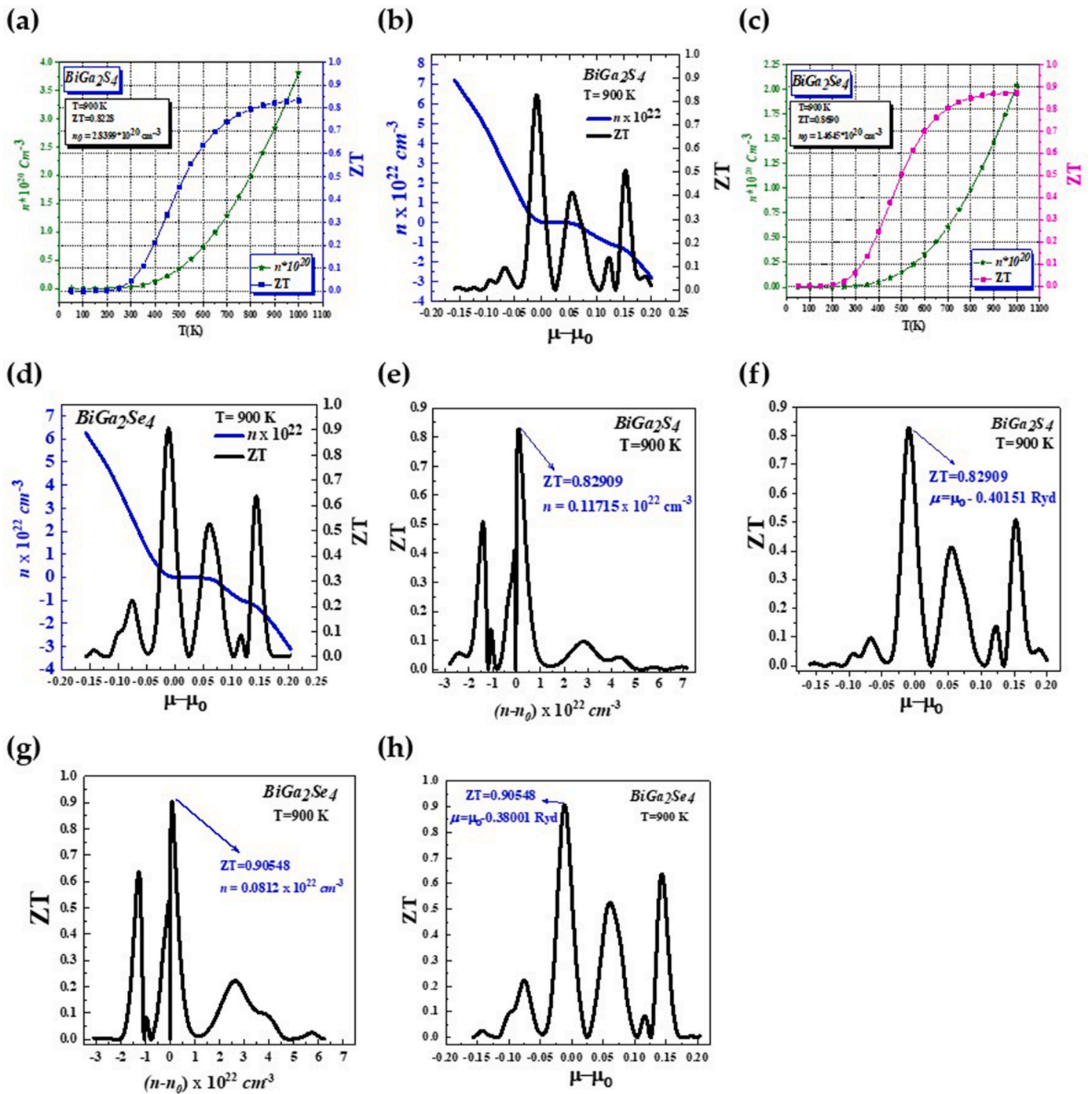
Fig. 10. The *ZT* of BiGa$_2$S$_4$ and BiGa$_2$Se$_4$ semiconductors when T = 900 K vs of (a), (c), (e), and (g), temperature and carrier concentration, (b), (d), (f), and (h), the chemical potentials.

sulfur-selenium *p-p* interactions. The gap is little affected by gallium's low-energy *s* and *p* bands. The maximum absorption along the x-axis occurs at 4.476 eV for *BiGa$_2$S$_4$* and 3.741 eV for *BiGa$_2$Se$_4$*. Additionally, *BiGa$_2$Se$_4$* has a higher dielectric constant. *BiGa$_2$S$_4$* and *BiGa$_2$Se$_4$* have zero-frequency refractive indices of (n_{xx} = 2.478, n_{zz} = 2.464), and (n_{xx} = 2.796, n_{zz} = 2.689), respectively, using the mBJ-LDA approximation. Calculations demonstrate that the real part and refractive index are somewhat anisotropic. *BiGa$_2$X$_4$* 's high absorption intensity makes it an important component for optoelectronic devices. The elastic properties show that our two materials are fragile and anisotropic. At 300 K: the k_L values for *BiGa$_2$S$_4$*, and *BiGa$_2$Se$_4$* are 1.57 W/mK, and 1.14 W/mK, and the Gruneisen values are γ (*BiGa$_2$S$_4$*) = 2.2298, and γ (*BiGa$_2$Se$_4$*) =

2.3098. Due to the comparatively low k_L at 400 K, the values of about 1.4710 W/(m.K), and 1.0101 W/(m.K) for *BiGa$_2$S$_4$*, and *BiGa$_2$Se$_4$*, respectively, are confirmed to be accurate. The Seebeck coefficients *S* for *BiGa$_2$S$_4$* and *BiGa$_2$Se$_4$* are 630.5726 μV/K and 543.4864 μV/K at 300 K. So, in *BiGa$_2$X$_4$* (*X = S, Se*) semiconductors, holes are likely the primary charge carriers, playing a crucial role in conduction. (σ/τ) was measured to be 0.0596 × 10^{18} (Ωms)$^{-1}$ for *BiGa$_2$S$_4$*, and 0.0755x10^{18} (Ωms)$^{-1}$ for *BiGa$_2$Se$_4$* at T = 300 K. At 1000 K, both *BiGa$_2$S$_4$*, and *BiGa$_2$Se$_4$* show significant ZT values of 0.8389 and 0.8722. The ZT values of the *p*-type semiconductors are much greater than those of the *n*-type. At 900 K, the *p*-type compound *BiGa$_2$S$_4$* has maximum ZT values of 0.8291 with 11.5565 × 10^{20} cm^3, the *p*-type compound *BiGa$_2$Se$_4$* has maximum

ZT values of 0.9054 with 8.11×10^{20} cm^3, respectively. At T = 300 K, the Seebeck coefficients of *BiGa$_2$S$_4$* and *BiGa$_2$Se$_4$* are (S_{xx} = 621.9488 μVK^{-1}, S_{zz} = 647.820 μVK^{-1}) and (S_{xx} = 580.51061 μVK^{-1}, S_{zz} = 469.43803 μVK^{-1}), respectively. (σ_{xx}) is 78.37 (61.59) percent at high temperatures for the semiconductor *BiGa$_2$S$_4$* (*BiGa$_2$Se$_4$*). At high temperatures, ($k_{e_{zz}}$) exceeds ($k_{e_{xx}}$) since ($k_{e_{xx}}$) is determined to be 84.4901 (94.660543) percent of that of ($k_{e_{zz}}$). The maximum ZT values for *BiGa$_2$S$_4$* and *BiGa$_2$Se$_4$* are shown to be 0.82909 and 0.90548, respectively. It is necessary to increase the concentration of charge carriers to n = 0.11715 x 10^{22} cm^{-3} for *BiGa$_2$S$_4$* and n = 0.0812 x 10^{22} cm^{-3} for *BiGa$_2$Se$_4$* to achieve this value. The chemical potentials of the semiconductors *BiGa$_2$S$_4$* and *BiGa$_2$Se$_4$* were both reduced by 0.40151 Ryd and 0.38001 Ryd, respectively, and the outcomes were identical.

CRediT authorship contribution statement

Ahmad Telfah: Writing – review & editing, Writing – original draft, Visualization, Investigation, Funding acquisition, Formal analysis, Conceptualization. **T. Ghellab:** Writing – review & editing, Writing – original draft, Visualization, Methodology. **Z. Charifi:** Writing – review & editing, Writing – original draft, Visualization, Software, Methodology, Investigation, Conceptualization. **H. Baaziz:** Writing – review & editing, Writing – original draft, Visualization, Validation, Methodology, Conceptualization. **A.M. Alsaad:** Writing – review & editing, Writing – original draft, Visualization, Investigation, Formal analysis, Data curation, Conceptualization. **Sahar Abdalla:** Writing – review & editing, Writing – original draft, Methodology, Formal analysis, Data curation, Conceptualization. **Wai-Ning Mei:** Writing – review & editing, Writing – original draft, Visualization, Validation, Conceptualization. **R. F. Sabirianov:** Writing – review & editing, Writing – original draft, Visualization, Investigation, Data curation, Conceptualization.

Declaration of competing interest

The authors declare that they have no known competing financial interests or personal relationships that could have appeared to influence the work reported in this paper.

Data availability

Data will be made available on request.

Acknowledgment

References

[1] See, https://www.nrel.gov/pv/assets/images/efficiency-chart.png/for/efficiency-chart.png, 2017. (Accessed 19 January 2018) (2219×1229.
[2] C. Wadia, A.P. Alivisatos, D.M. Kammen, Environ. Sci. Technol. 43 (2009) 2072–2077.
[3] P.C.K. Vesborg, T.F. Jaramillo, RSC Adv. 2 (2012) 7933.
[4] M. Liu, et al., Nat. Mater. 16 (2017) 258–263.
[5] E.M. Sanehira, et al., Sci. Adv. 3 (2017) eaao4204.
[6] W.S. Yang, et al., Science 356 (2017) 1376–1379.
[7] WHO, Ten Chemicals of Major Public Health Concern, WHO, 2016.
[8] A. Babayigit, H.-G. Boyen, B. Conings, MRS Energy Sustain. 5 (2018) E1.
[9] J.L. DiMeglio, J. Rosenthal, J. Am. Chem. Soc. 135 (2013) 8798–8801.
[10] R. Mohan, Nat. Chem. 2 (2010) 336.
[11] A.M. Ganose, C.N. Savory, D.O. Scanlon, Chem. Commun. 53 (2017) 20–44.
[12] R.E. Brandt, V. Stevanovi, D.S. Ginley, T. Buonassisi, MRS Commun. 5 (2015) 265–275.
[13] D. M. Rowe, Boca Raton, FL, USA: CRC Press (2018). doi:10.1201/9781420038903.
[14] G.J. Snyder, E.S. Toberer, Mater. Sci. Eng. 7 (2010) 101–110, https://doi.org/10.1142/9789814317665_0016.
[15] G.H. Carey, a.L. Abdelhady, Z. Ning, S.M. Thon, O.M. Bakr, E.H. Sargen, Chem. Rev. 115 (2015) 12732–12763.
[16] F. Liu, C. Ding, Y. Zhang, T.S. Ripolles, T. Kamisaka, T. Toyoda, S. Hayase, T. Minemoto, K. Yoshino, S. Dai, M. Yanagida, H. Noguchi, Q. Shen, J. Am. Chem. Soc. 139 (2017) 16708.
[17] M. Yuan, M. Liu, E.H. Sargent, Nat. Energy 1 (2016) 16016.
[18] C.R. Kagan, C.B. Murray, Nat. Nanotechnol. 10 (2015) 1013–1026.
[19] J. Chao, et al., Mater. Res. Bull. 98 (2018) 194–199.
[20] W. Huang, et al., Nanoscale 10 (2018) 2404–2412.
[21] H. Yu, et al., CrystEngComm 19 (2017) 727–733.
[22] A. Sarkar, et al., J. Colloid Interface Sci. 483 (2016) 49–59.
[23] X. Meng, Z. Zhang, J. Mol. Catal. Chem. 423 (2016) 533–549.
[24] H. Abdullah, D.-H. Kuo, J. Phys. Chem. C 119 (2015) 13632–13641.
[25] J. Ni, et al., Adv. Energy Mater. 4 (2014) 1400798.
[26] G. Nie, X. Lu, J. Lei, L. Yang, C. Wang, Electrochim. Acta 154 (2015) 24–30.
[27] W. Yang, H. Wang, T. Liu, L. Gao, Mater. Lett. 167 (2016) 102–105.
[28] K. Biswas, L.D. Zhao, M.G. Kanatzidis, Adv. Energy Mater. 2 (2012) 634–638.
[29] Y. Cheng, et al., Angew. Chem., Int. Ed. 57 (2018) 246–251.
[30] Y. Yang, et al., Part. Syst. Charact. 32 (2015) 668–679.
[31] Z. Li, et al., RSC Adv. 7 (2017) 29672–29678.
[32] S. Johnsen, Z. Liu, J.A. Peters, J.-H. Song, S.C. Peter, C.D. Malliakas, N.K. Cho, H. Jin, A.J. Freeman, B.W. Wessels, M.G. Kanatzidis, Chem. Mater. 23 (2011) 3120–3128.
[33] P.L. Wang, Z. Liu, P. Chen, J.A. Peters, G. Tan, J. Im, W. Lin, A.J. Freeman, B. W. Wessels, M.G. Kanatzidis, Adv. Funct. Mater. 25 (2015) 4874–4881.
[34] J. Wei, L. Yang, Z. Ma, et al., J. Mater. Sci. 55 (2020) 12642–12704, https://doi.org/10.1007/s10853-020-04949-0.
[35] Z. Ma, J. Wei, P. Song, M. Zhang, L. Yang, J. Ma, W. Liu, F. Yang, X. Wang, Mater. Sci. Semicond. Process. 121 (2021) 105303, https://doi.org/10.1016/j.mssp.2020.105303.
[36] G. Nazir, Q. Mahmood, T. Zelai, A. Rehman, H. Albalawi, N.A. Kattan, S. Bouzgarrou, I. Boukhris, Phys. Scripta 99 (5) (2024), https://doi.org/10.1088/1402-4896/ad3c7d. Article 055972.
[37] R.M. Arif Khalil, Muhammad Iqbal Hussain, Mushahid Hussain Shah, Tahani I. Al-Muhimeed, Ghazanfar Nazir, Fayyaz Hussain, Umair Mumtaz, Comput. Mater. Sci. 238 (2024) 112947.
[38] Ghazanfar Nazir, Ayman S. Alofi, Adeela Rehman, Q. Mahmood, Murefah mana Al-Anazy, Rachid Karmouch, Md Ferdous Rahman, El Sayed Yousef, Mater. Sci. Semicond. Process. 173 (2024) 108129.
[39] Ghazanfar Nazir, Q. Mahmood, Adeela Rehman, Ayman S. Alofi, Hind Albalawi, Taharh Zelai, Hakami Othman, A.I. Aljameel, N. Safina, El Sayed Yousef, J. Phys. Chem. Solid. 184 (2024) 111740.
[40] Kanwal Majeed, Muhammad Azhar Khan, Raqiqa Tur Rasool, Shagufta Gulbadan, Abeer A. AlObaid, M. Irfan::ce:given-name)> Irfan , Ghulam Abbas Ashraf, Ghazanfar Nazir, Majid Niaz Akhtar, Mater. Chem. Phys. 306 (2023) 128061.
[41] P. Blaha, K. Schwarz, G.K. Madsen, D. Kvasnicka, J. Luitz, wien2k. An Augmented Plane Wave+ Local Orbitals Program for Calculating Crystal Properties, Vienna University of Technology, Vienna, 2001.
[42] J.P. Perdew, Y. Wang, Phys. Rev. B 45 (1992) 13244–13249.
[43] F. Tran, P. Blaha, Phys. Rev. Lett. 102 (2009) 226401.
[44] D.J. Singh, Phys. Rev. B 82 (20) (2010) 205102.
[45] J. Camargo-Martínez, R. Baquero, Phys. Rev. B 86 (19) (2012) 195106.
[46] F. Tran, P. Blaha, Phys. Rev. Lett. 102 (22) (2009) 226401.
[47] G.K.H. Madsen, D.J. Singh, Comput. Phys. Commun. 175 (2006) 67–71.
[48] H. Kalpen, W. Honle, M. Somer, U. Schwarz, K. Peters, H. Georg von Schnering, Z. Anorg. Allg. Chem. (1998) 624.
[49] F.D. Murnaghan, Proc. Nat. Acad. Sci. USA 30 (1944) 244.
[50] O.K. Anderson, Phys. Rev. B 12 (1975) 3060.
[51] W. Shan, W. Walukiewicz, J.W. Ager III, E.E. Haller, J. F. Geisz, D. J. Friedman, J. M.
[52] D.R. Penn, Phys. Rev. B 128 (1962) 2093.
[53] T. Ghellab, H. Baaziz, Z. Charifi, K. Bouferrache, M.A. Saeed, A. Telfah, Mater. Res. Express 6 (2019) 075906.
[54] T. Ghellab, Z. Charifi, H. Baaziz, Ş. Uğur, G. Uğur, F. Soyalp, Phys. Scripta 91 (2016) 045804.
[55] T. Ghellab, Z. Charifi, H. Baaziz, K. Bouferrache, B. Hamad, Int. J. Energy Res. (2019) 1–15.
[56] L. Shi, J. Hu, Y. Qin, Y. Duan, X Yang Lwu, J. G Tang, Alloys Compounds 611 (2014) 210.
[57] J.B. Levine, S.H. Tolbert, R.B. Kaner, Adv. Funct. Mater. 19 (2009) 3519.
[58] W. Voigt, Lehrbuch der Kristallphysik, second ed., Teubner, 1910 (*Leipzig and Berlin: B.G).* [*reprinted in* (1928)].
[59] A. Reuss, Z. Angew. Math. Mech. 9 (1929) 49.
[60] R. Hill, Proc. R. Soc. Lond. Ser. A 65 (1952) 349.
[61] S.F. Pugh, Philos. Mag. A 45 (1954) 823.
[62] H. Fu, D. Li, F. Peng, T. Gao, X. Cheng, J. Alloys Compd. 473 (2009) 255.
[63] P. Ravindran, L. Fast, P.A. Korzhavyi, B. Johansson, J. Appl. Phys. 84 (1998) 4891.
[64] V.V. Bannikov, I.R. Shein, A.L. Ivanovskii, J. Alloys Compd. 533 (2012) 71.
[65] D.H. Chung, W.R. Buessem, Anisotropy in single crystal refractory compound, in: F. W. Vahldiek, S.A. Mersol (Eds.), Plenum 2 (217) (1968). New York.
[66] S.I. Ranganathan, M. Ostoja-Starzewski, Phys. Rev. Lett. 101 (2008) 055504.
[67] A. Cazzani, M. Rovati, Inter J. Of Solid and Struc vol. 42 (2005) 5057–5096.

[68] P. Wachter, M. Filzmoser, J. Rebiant, Physica B 293 (2001) 199.
[69] W. Voigt, Semiconductors and semimetals. *Lehrbuch der Kristall-physik (Leipzing, Taubner)*, 1929.
[70] E. Schreiber, O.L. Anderson, N. Soga, Elastic Constants and Their Measurements, McGraw-Hill, New York, 1973.
[71] G.K. Madsen, J. Carrete, M.J. Verstraete, Comput. Phys. Commun. 231 (2018) 140–145.
[72] D.T. Morelli, G.A. Slack, in: S.L. Shindé, , et al.J.S. Goela (Eds.), High Thermal Conductivity Materials, Springer, New York, 2006, p. 37.
[73] C.L. Julian, Phys. Rev. A128 (1965) 137.
[74] A. Bulusu, D.G. Walker, Superlattice. Microst. 44 (2008) 1.
[75] T. Fang, S. Zheng, H. Chen, H. Cheng, L. Wang, P. Zhang, RSC Adv. 6 (2016) 10507.
[76] M. Matougui, et al., Chin. J. Phys. 57 (2019) 195.
[77] Z.A.A.R. Almaghbash, et al., Int. J. Thermophys. 42 (2021) 5.
[78] J. Yang, H. Li, T. Wu, W. Zhang, L. Chen, J. Yang, Adv. Funct. Mater. 18 (2008) 2880–2888.
[79] H. Kara, M. Upadhyay Kahaly, K. Özdoğan, J. Alloys Compd. 735 (2018) 950–958.
[80] H. Ma, C.-L. Yang, M.-S. Wang, X.-G. Ma, Y.-G. Yi, J. Phys. D Appl. Phys. 52 (2019) 255501.
[81] T. Ghellab, H. Baaziz, Z. Charifi, M. Telfah, A. Alsaad, A. Telfah, R. Hergenroder, R. Sabirianov, Mater. Sci. Semicond. Process. 141 (2022) 106415.
[82] T. Ghellab, H. Baaziz, Z. Charifi, K. Bouferrache, Ş. Uğur, G. Uğurand, H. Ünver, Int. J. Mod. Phys. B 33 (2019) 1950234.
[83] T. Ghellab, H. Baaziz, Z. Charifi, K. Bouferrache, M.A. Saeed, A. Telfah, Mater. Res. Express 6 (2019) 075906.
[84] I. Mili, H. Latelli, T. Ghellab, Z. Charifi, H. Baaziz, F. Soyalp, Int. J. Mod. Phys. B 35 (7) (2021) 2150100.
[85] A. Telfah, T. Ghellab, H. Baaziz, Z. Charifi, A.M. Alsaad, R. Sabirianov, J. Magn. Magn Mater. 562 (2022) 169822.
[86] Z. Charifi, T. Ghellab, H. Baaziz, F. Soyalp, Int. J. Energy Res. (2022) 1–19, https://doi.org/10.1002/er.8104.
[87] T. Ghellab, H. Baaziz, Z. Charifi, H. Latelli, Phys. B Condens. Matter 653 (2023) 414678, https://doi.org/10.1016/j.physb.2023.414678.